

Modeling the recent interactions between the Magellanic Clouds and Milky Way

Bethany R. Garver,¹★ David L. Nidever,^{1,2} Victor P. Debattista,³† Nathan Deg⁴

¹Department of Physics, Montana State University, P.O. Box 173840, Bozeman, MT 59717-3840

²Center for Computational Astrophysics, Flatiron Institute, 162 Fifth Avenue, New York, NY 10010, USA

³Jeremiah Horrocks Institute, University of Lancashire, Preston, PR1 2HE, UK

⁴Department of Physics, Engineering Physics, and Astronomy, Queen's University, Kingston ON K7L 3N6, Canada

arXiv:2602.05021v1 [astro-ph.GA] 4 Feb 2026

Accepted XXX. Received YYY; in original form ZZZ

ABSTRACT

The Large and Small Magellanic Clouds (LMC and SMC, respectively) are the largest satellite galaxies of the Milky Way (MW) and their interactions with each other have given rise to multiple stellar substructures in their periphery as well as the gaseous Magellanic Stream. To better understand the origin of the stellar substructures and constrain their past orbit, we model the past 2.5 Gyr of the interactions between the MW and the LMC and SMC using N-body simulations. Due to the strong interactions, analytical orbit integrations are insufficient to analyze the past galaxy orbits accurately. Therefore, we use a genetic algorithm in combination with N-body simulations to determine the LMC and SMC initial positions and velocities 2.5 Gyr ago that result in the Magellanic Clouds (MCs) arriving near their observed locations and velocities at the current time. After running ~8,000 simulations, our best matching model includes two close interactions between the MCs (940 Myr and 140 Myr ago) and reproduces some observed features of the MCs, including the LMC disc warp, a ring-shaped overdensity in the LMC, the tidal expansion of the SMC, and a greater distance dispersion on the eastern side of the SMC. The LMC disc warp is caused by the most recent interaction with the SMC, which occurred ~140 Myr before the present. The interaction causes global ripples in the LMC disc with a mean amplitude of 1.3 kpc.

Key words: Magellanic Clouds – galaxies: interactions

1 INTRODUCTION

The Large Magellanic Cloud (LMC) and Small Magellanic Cloud (SMC) are nearby galaxies interacting with each other and with the Milky Way (MW). Their structure has been studied for decades with optical and near-infrared (NIR) photometry (e.g., [van der Marel 2001](#); [Mackey et al. 2016](#); [Nidever et al. 2017](#)), optical/NIR spectroscopy (e.g., [van der Marel et al. 2002](#); [Carrera et al. 2008](#); [Nidever et al. 2020](#)), UV ([Hagen et al. 2017](#)), H α ([Barger et al. 2013](#)), radio continuum (e.g., [Klein et al. 1993](#); [Filipovic et al. 1998](#)), molecular gas (e.g., [Wong et al. 2011](#)), 21cm HI (e.g., [Putman et al. 2003](#); [Nidever et al. 2008](#)), and more.

Recent wide-field surveys and spectroscopic studies have revealed that the Magellanic Clouds host a wealth of substructure, providing strong evidence of their dynamic interaction history. [Majewski et al. \(2009\)](#) and [Nidever et al. \(2011\)](#) used pencil-beam Washington+*DDO*51 photometry with follow-up spectroscopy of giant stars to discover evidence for very extended stellar components around the MCs (LMC: $R \approx 20^\circ$, SMC: $R \approx 12^\circ$). [Saha et al. \(2010\)](#) used deep photometry to track main-sequence turnoff (MSTO) stars out to a radius of $\sim 16^\circ$ to the north. [Mackey et al. \(2016\)](#) first mapped the northern stream of the Large Magellanic Cloud (LMC), and subse-

quent work with deeper imaging revealed that this structure extends even farther ([Belokurov & Erkal 2019](#)) and includes two distinctive southern ‘hook’-shaped features ([Mackey et al. 2018](#)). Using red clump stars from the Survey of the Magellanic Stellar History (SMASH; [Nidever et al. 2017, 2021](#)), [Choi et al. \(2018a,b\)](#) mapped the three-dimensional geometry of the LMC disc and uncovered a pronounced southern warp extending roughly 4 kpc below the disc plane in the direction of the Small Magellanic Cloud (SMC). [Saroor & Subramanian \(2022\)](#) later identified a northern warp with *Gaia* DR2 data that bends in the same direction, giving the LMC disc a ‘U’-shaped morphology—an unexpected feature if the distortion were purely tidal in origin. In addition, the outer stellar density profile of the LMC shows significant irregularities. [Nidever et al. \(2019a\)](#) found that while the overall profile can be described by a double-exponential or exponential-plus-power-law form, there is considerable scatter about the best-fitting model, indicating substantial substructure in the outskirts. Kinematically, [Olsen et al. \(2011\)](#) uncovered a population of metal-poor, counter-rotating stars in the LMC, providing further evidence for past interactions or accretion events. Finally, [Nidever et al. \(2020\)](#) used SDSS-IV / APOGEE-2S ([Majewski et al. 2017](#)) high-resolution spectroscopy to map the chemical enrichment of both Clouds, finding similarly low $[\alpha/\text{Fe}]$ ‘knees’ at $[\text{Fe}/\text{H}] \approx -2.2$ and evidence for recent starburst activity, further linking the Clouds’ chemical evolution to their dynamical interaction history.

★ E-mail: bethanygarver@montana.edu

† E-mail: vpdebattista@lancashire.ac.uk

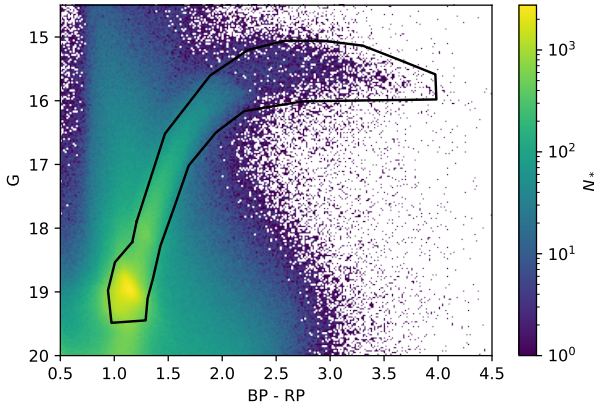


Figure 1. Color magnitude diagram of *Gaia* EDR3 MC stars. The black boundary shows the cuts we use for MC red clump and red giant branch stars.

The SMC exhibits a similarly complex structure, with both its morphology and kinematics bearing clear signatures of tidal influence from the LMC. Early photographic studies revealed a distance bimodality in the eastern SMC (Hatzidimitriou & Hawkins 1989), later confirmed with deep photometric data by Nidever et al. (2013), who found that the more distant eastern component resembles the central and western regions of the SMC, while the nearer eastern component consists of tidally stripped material. Spectroscopic evidence supports this picture with Almeida et al. (2024) showing that the distant eastern stars have a metallicity distribution function (MDF) similar to that of the western population, whereas the near eastern stars are more metal-rich, resembling the central SMC population—consistent with their origin as recently stripped stars. The SMC also possesses extended stellar features, including the SMC Northern Overdensity (SMCNOD), discovered by Pieres et al. (2017) using DES data (Dark Energy Survey Collaboration et al. 2016), located roughly 8° from the SMC center. The timing and geometry of these features provide important constraints on the most recent close encounter between the Clouds. Choi et al. (2022) used *Gaia* measurements of LMC disc distortions to infer the timing and impact parameter of this interaction. Observational constraints from *Gaia* DR2, including proper motions and radial velocities of red giant stars, were used by Zivick et al. (2021) to model SMC kinematics, revealing a modest intrinsic rotation of $\sim 10\text{--}20 \text{ km s}^{-1}$ and a tidal expansion component of $\sim 10 \text{ km s}^{-1} \text{ kpc}^{-1}$. Massana et al. (2024) used *Gaia* XP stellar parameters from Andrae et al. (2023) to map metallicities across the MCs and found that both the SMC-NOD and its southern counterpart, the SMC Southern Overdensity (SMCSOD), are metal-poor with MDFs similar to those in the SMC outskirts. Together, these discoveries paint a picture of a dynamically active Magellanic system, where repeated interactions between the LMC and SMC have produced tidal warps, streams, and extended stellar envelopes.

Simulations of the Magellanic Clouds have progressed from early low-resolution N-body approaches (e.g., Lin & Lynden-Bell 1977; Kunkel 1979; Murai & Fujimoto 1980) to modern hydrodynamical models that incorporate detailed Milky Way interactions and internal cloud dynamics. Růžička et al. (2010) performed a broad parameter-space search using a genetic algorithm (Wahde 1998; Theis 1999) with test-particle simulations, providing some initial constraints on the orbital and interaction history of the Clouds. Connors et al. (2006) N-body simulations reproduced the Leading Arm and the two filaments of the trailing Stream using tidal interactions between the MCs

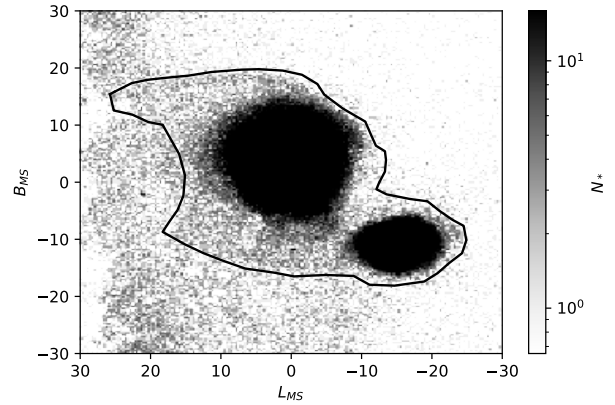


Figure 2. Density map of *Gaia* MC giant stars. The black line shows the selection we used on the map of the stars on Magellanic Stream coordinates L_{MS} and B_{MS} .

and MW. After Besla et al. (2007) discovered that the MCs are very likely on their first infall into the MW, a newer generation of simulations by Besla et al. (2012) and Diaz & Bekki (2012) explored the interactions between the LMC and SMC and were able to reproduce key features of the Magellanic Stream, including its bifurcated filamentary structure and predicted the SMC ‘counterbridge’.

Hydrodynamical simulations have further illuminated the role of gas physics in shaping the Magellanic system. Lucchini et al. (2020) included a hot Magellanic corona in their models, which shields leading gas from ram pressure stripping by the MW halo and naturally produces the observed Leading Arm Feature (LAF; Putman et al. 1998; Brüns et al. 2005). While Lucchini et al. (2021) suggested that the trailing Magellanic Stream could lie as close as ~ 20 kpc, recent stellar detections within the Stream at ~ 100 kpc (Zaritsky et al. 2020; Chandra et al. 2023) indicate a greater distance. Supporting these models, Price-Whelan et al. (2019) and Nidever et al. (2019b) identified a young (117 Myr) star cluster in the MW formed from Leading Arm gas.

Comprehensive simulation suites such as KRATOS (Jiménez-Arranz et al. 2024), and the studies by Sheng et al. (2024) and Lucchini et al. (2024) explore a wide range of parameters including halo masses, corona properties, and orbital histories, providing frameworks to reproduce both the large-scale gaseous features and the complex stellar substructures observed today. Additionally, Vasiliev (2024) demonstrated methods for evolving an LMC within a Milky Way potential while recovering key kinematic and structural properties, offering a practical approach to connecting simulations with observations. However, reliably reconstructing the orbital history of the MCs that models their interactions accurately and reproduces their current positions, velocities and substructures remains challenging and elusive. In particular, their close interactions are challenging to model analytically because of the strong dynamical friction and tidal distortions.

Here, we attempt to tackle the challenge of recovering the complex recent interaction history of the MCs as well as their stellar substructures with a large suite of N-body simulations. In Section 2, we discuss the *Gaia* and APOGEE datasets used for observational comparison. The simulations are described in Section 3 and details of setting up the interactions and genetic algorithm are provided in Section 4. A detailed comparison of our simulations with observed features is given in Section 5. Finally, we discuss the implications of our work in Section 6 and provide our conclusions in Section 7.

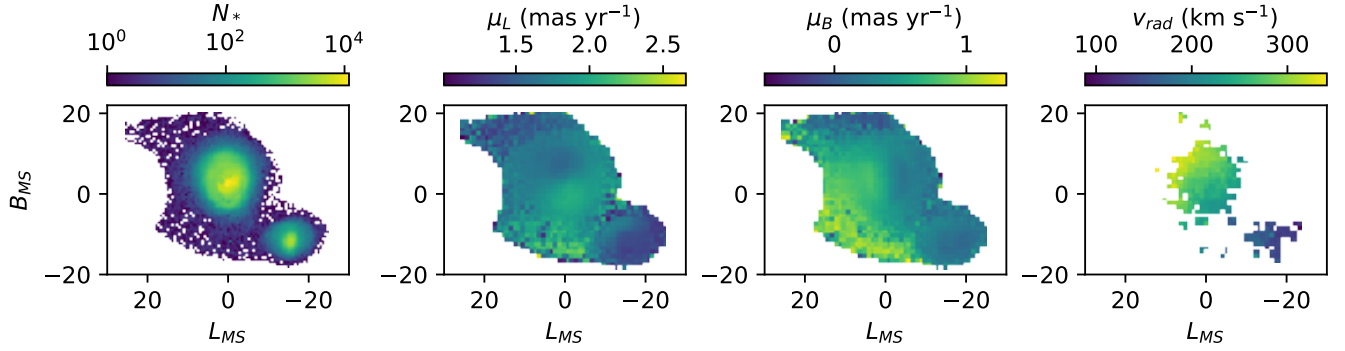


Figure 3. Maps of the observed *Gaia* and SDSS MC data. *left*: Number of stars, *center left*: mean proper motion in the L_{MS} direction, *center right*: mean proper motion in the B_{MS} direction, and *right* mean line-of-sight velocity.

2 DATA

The observational data we use to generate the MC proper motion and density maps come from *Gaia* EDR3 (Gaia Collaboration et al. 2021a), while the radial velocity measurements come from SDSS-IV / APOGEE DR17 (Abdurro'uf et al. 2022). To filter the *Gaia* data, we use a process similar to what is described by Belokurov & Erkal (2019). A CMD filter is applied to select MC red clump (RC) and red giant branch (RGB) stars, as shown in Figure 1. In addition, stars with proper motions outside the range of $0.9 \leq \mu_{L_{\text{MS}}} \leq 2.8 \text{ mas yr}^{-1}$ and $-0.6 \leq \mu_{B_{\text{MS}}} \leq 1.4 \text{ mas yr}^{-1}$ are removed, where $\mu_{L_{\text{MS}}}$ and $\mu_{B_{\text{MS}}}$ are proper motions in the Magellanic Stream (MS) coordinate system (Nidever et al. 2008). Foreground stars are also removed with a parallax cut $\varpi > 0.2$. Finally, we select stars in $L_{\text{MS}}-B_{\text{MS}}$ space to include the main stellar features of the interaction between the MCs (see Figure 2). The observational maps of density, proper motions, and radial velocities are shown in Figure 3.

3 SIMULATIONS

We model the interactions between the MW and MCs using N-body simulations evolved with the PKDGRAV software package (Stadel 2001). PKDGRAV is a highly efficient, fully parallel N-body code that employs adaptive spatial and temporal resolution as well as a k-D tree-based force algorithm to enable large cosmological simulations for studying galaxy formation. Low-resolution simulations are used with the genetic algorithm for improved speed. Subsequently, a variety of higher-resolution simulations are performed for the best-fitting orbit.

For the low-resolution N-body simulations used with the genetic algorithm, the three galaxies are initialized as follows: The LMC is modeled with 1.62×10^5 star particles and 2.38×10^5 dark matter particles. The assumed stellar mass of the LMC is $7.20 \times 10^9 M_{\odot}$ and the dark matter halo has a mass of $1.76 \times 10^{11} M_{\odot}$ (Erkal et al. 2019). The stellar mass is higher than the observed value of $2.7 \times 10^9 M_{\odot}$ (Besla 2015) because it includes the gas mass as well as mass that has been stripped from the LMC in the past few Gyr. The SMC has 2.25×10^4 star particles and 2.9×10^4 dark matter particles. Its stellar mass is $1.06 \times 10^9 M_{\odot}$ and its dark matter halo is $2.02 \times 10^{10} M_{\odot}$ (Besla et al. 2012). The MW has 2.4×10^4 star particles and 2.5×10^4 dark matter particles. Its stellar mass is $5.25 \times 10^{10} M_{\odot}$ and its dark matter halo has mass $1.16 \times 10^{12} M_{\odot}$. These three models are each evolved in isolation for 6 Gyr. The ‘evolved’ galaxies are then used as

inputs for the genetic algorithm simulations where all three combined are run for another 2.5 Gyr.

After running the genetic algorithm, we use 10× higher resolution LMC, SMC, and MW models. The higher resolution makes it easier to find features in the MCs while having minimal effect on the orbits. In simulations comparing the orbits of the LMC with the lower and higher resolution MWs, the final LMC locations are less than 2 kpc apart.

In addition to our fiducial high-resolution LMC model (model A), we run the simulation with the same initial positions and velocities for five other LMC models: B, which has a thicker disc, C, which has a thinner disc, D, which has a hotter disc, F, which has a more compact dark matter halo, and G, which has a more diffuse dark matter halo. The properties of these models and the SMC model are given in Table 1.

4 METHODS

We run simulations with just the LMC and SMC, as well as simulations that include both MCs and the MW. For both groups of simulations, we save snapshots every 20 Myr and calculate the median particle position and velocity for the LMC and SMC. The median is used rather than the center of mass because it is less sensitive to outliers. We compare these values to the observed center of mass (COM) positions and velocities shown in Table 2. The LMC velocity comes from Kallivayalil et al. (2013) and the SMC velocity comes from Zivick et al. (2018).

In both groups of simulations, we use a genetic algorithm in which we vary the initial positions, velocities, and orientations of the simulated MCs and compare them to the observed COM positions and velocities, as well as density, proper motions in the L_{MS} and B_{MS} directions, and radial velocities at the ‘current’ time. The current time is defined when the LMC center reaches $L_{\text{MS}}=0^{\circ}$, with the Sun at the position of $(X, Y, Z)=(-8.0 \text{ kpc}, 0.0 \text{ kpc}, 0.0 \text{ kpc})$ in the MW-centric frame.

4.1 Genetic Algorithm

We employ a genetic algorithm to thoroughly and efficiently explore the 9-dimensional parameter-space of initial conditions that produces the best-fitting final LMC/SMC positions and velocities. A genetic algorithm is a stochastic optimization technique that explores

| Model | M_h ($10^{11} M_\odot$) | R_h (kpc) | σ_h (km s $^{-1}$) | M_d ($10^9 M_\odot$) | R_d (kpc) | Z_d (kpc) | σ_R (km s $^{-1}$) |
|-------|--------------------------------|----------------|-------------------------------|-----------------------------|----------------|----------------|-------------------------------|
| LMC A | 1.76 | 21.4 | 222 | 7.20 | 2 | 0.28 | 45 |
| LMC B | 1.75 | 21.4 | 222 | 7.20 | 2 | 0.41 | 45 |
| LMC C | 1.77 | 21.4 | 222 | 7.20 | 2 | 0.22 | 45 |
| LMC D | 1.76 | 21.4 | 222 | 7.20 | 2 | 0.28 | 56.25 |
| LMC F | 1.76 | 13 | 237 | 7.20 | 2 | 0.28 | 45 |
| LMC G | 1.76 | 32 | 216 | 7.20 | 2 | 0.28 | 45 |
| SMC | 0.202 | 7.3 | 125 | 1.06 | 1.4 | 0.26 | 20 |

Table 1. Properties of the different LMC models and the SMC model we use.

| Galaxy | Observed Position (x, y, z) [kpc] | Observed Velocity (v_x, v_y, v_z) [km s $^{-1}$] |
|--------|--|--|
| LMC | ($-1.0, -40.9, -27.7$) | ($-57 \pm 13, -226 \pm 15, 221 \pm 19$) |
| SMC | ($14.9, -38.1, -44.2$) | ($18 \pm 6, -179 \pm 16, 174 \pm 13$) |

Table 2. The observed positions and velocities that we compare to the simulations.

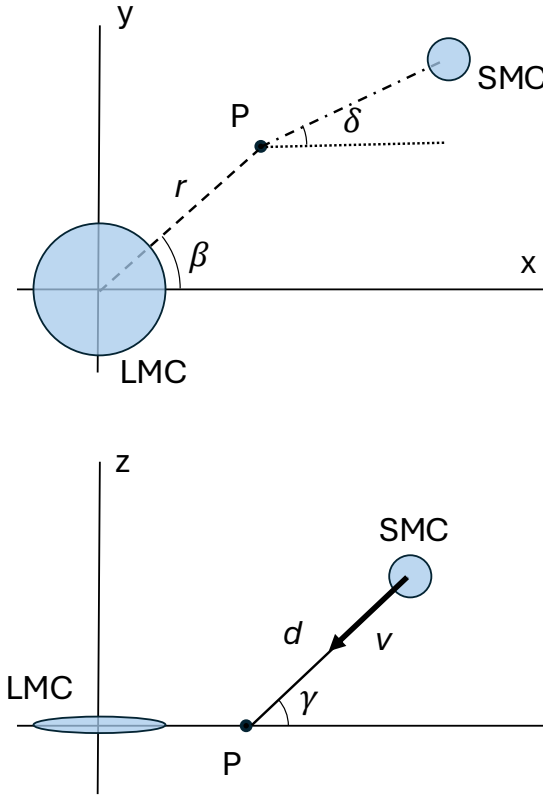


Figure 4. Diagram of the coordinates we define for our two-galaxy simulations. *Top:* projection onto the $x - y$ plane. *Bottom:* projection onto the plane perpendicular to the $x - y$ plane that includes the initial location of the SMC center and point P.

parameter space by mimicking natural selection, evolving a population of candidate solutions through operations such as mutation, crossover, and selection to efficiently converge toward an optimal or near-optimal parameters. For each ‘generation’ of solutions (i.e., the initial conditions), fifteen simulations are run at a time. Their ‘fitness’ (or goodness-of-fit) is calculated by comparing the simulated positions and velocities of the LMC and SMC at the current time (the snapshot nearest to when the LMC crosses the Magellanic longitude of 0) with the observed values.

$$\text{fitness} = 1 / \sqrt{\Delta d_{\text{LMC}}^2 + \Delta d_{\text{SMC}}^2 + \Delta v_{\text{LMC}}^2 + \Delta v_{\text{SMC}}^2} \quad (1)$$

where Δd and Δv are unnormalized differences in the simulated and observed 3-D positions and space velocities, respectively. Simulations where the LMC and SMC have merged are downweighted by cutting the fitness value in half for any simulations where the LMC and SMC are less than 15 kpc apart at the time the LMC crosses $L_{MS} = 0$. We tested incorporating comparisons to maps of stellar density, radial velocity, and proper motion in both Magellanic longitude and latitude. However, this did not have much of an effect compared to the central positions and velocities of the galaxies.

The solutions for the next generation are produced with a combination of crossover and mutation. Two solutions are selected with weighted random sampling with a probability proportional to their fitness (‘fitter’ solutions are more likely to be selected for a pair) and their values averaged. Randomly distributed noise is then added to these values with a Gaussian sigma of 0.5 kpc for the LMC position, 1 km s $^{-1}$ for the LMC velocity, 1 kpc for the SMC position, and 2 km s $^{-1}$ for the SMC velocity. The orientation of the LMC and the galaxy masses are held fixed. The best-fitting solution of each iteration is always kept to the next iteration.

4.2 Two-galaxy simulations

Initially, we modeled the recent interactions of the MCs using simulations of just the LMC and SMC without the Milky Way, focusing on the recent close interaction. In the end, these simulations failed to provide a good match for our chosen comparison features. Therefore, we moved on to simulations that also included the MW which are described in the next section. However, it is instructive to describe the two-galaxy simulations.

For our simulations involving only the LMC and SMC, we defined a coordinate system that describes the initial locations of the MCs relative to each other as well as where the SMC would first cross the plane of the LMC disc if it were to travel in a straight line. The LMC was placed at the origin with its disc in the $x - y$ plane and defined coordinates as follows: r is the distance from the LMC center to the point, P, where the SMC’s path would cross the LMC disc plane if

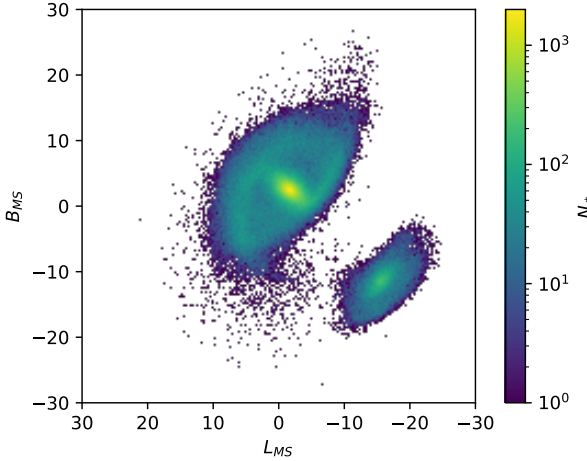


Figure 5. The LMC and SMC at the end of a two-galaxy simulation.

it were moving in a straight line, d is the distance from the SMC center to P, v is the initial speed of the SMC, β is the angle from the x -axis counterclockwise to P, δ is the angle counterclockwise of the projection of the SMC's path onto the $x - y$ plane from the x -axis, and γ is the angle of the SMC's path above or below the $x - y$ plane. The diagrams in Figure 4 illustrate the coordinates.

The two galaxies are evolved for 2 Gyr with PKDGRAV. At the end of each of simulation, the particles are translated so that the center of the simulated LMC is at its current observed coordinates and orientation. In addition, the simulated particles are rotated about the LMC's axis so that the SMC is at its observed orientation angle from our perspective. This allows us to find the locations of the MCs as they would appear in the sky. An example of such a simulation is shown in Figure 5.

We used a genetic algorithm of simulations where we varied the parameters defined above. A total of 4830 simulations were run, however, the final solutions were not satisfactory. In simulations where the SMC ended up closest to its observed position, its velocity was never closer than 75 km s^{-1} from its observed value. We concluded that the MW's influence on the MCs was an important component that could not be approximated away by this two-galaxy approach.

4.3 Three-galaxy simulations

Next, we modeled the three-galaxy MW-LMC-SMC system with each component being 'live' and modeled as N-body star and dark matter particles. To find the initial positions and velocities for the model including the MW, we used GALA (Price-Whelan 2017; Price-Whelan et al. 2023) run back in time for 2.5 Gyr with MW, LMC, and SMC potentials. The potentials we used for each galaxy in GALA had the same mass for each component as we used with PKDGRAV above and matched the radial profiles as well. To accomplish this, we used a separate disc and halo component for each galaxy and adjusted their sizes and masses to match the N-body models. Figure 6 compares radial potentials of our GALA potentials to the PKDGRAV N-body models. To account for dynamical friction, which is significant in the closely interacting galaxies, we used Equations 8.2 and 8.7 from Binney & Tremaine (2008) to calculate the appropriate approximation to the acceleration. We have dynamical friction from the MW acting on both MCs and dynamical friction from the LMC acting on the SMC.

As shown in Figure 7, the orbits recovered with GALA are close to,

but not exactly like, the orbits with PKDGRAV. Part of this disparity is due to the fact that the dynamical friction approximation fails when the MCs closely interact. In an attempt to mitigate this, we increased the dynamical friction on the SMC by the LMC by a factor of seven, which improved the agreement with PKDGRAV somewhat. Even with our ad hoc adjustments to the dynamical friction, the differences in the GALA and PKDGRAV orbits were significant enough that using GALA to determine the best initial conditions was not a viable solution. The increase in dynamical friction, while overall helping the orbits match those found with PKDGRAV, caused us to overestimate the later dynamical friction between the MCs, because the halos do not strip with GALA. Therefore, we again used a genetic algorithm as with the two-galaxy simulations to find the best initial conditions. We varied the initial positions (x , y , and z) and velocities (v_x , v_y , and v_z) of both MCs.

After running each simulation, the MW is centered and all particles are rotated about the axis of the MW until the LMC is at its observed angle on the $x - y$ plane. Then we find the snapshot in the last 500 Myr where the center of the LMC is the closest to $L_{\text{MS}} = 0^\circ$. This is not necessarily the snapshot with the highest fitness because it does not take the SMC into account but for the purpose of our analysis, we want the LMC to be as close to its observed location as possible. Finally, fitness is calculated based on how well both MC median positions and velocities match the observed values from Table 2.

In addition, the distances between the MCs are tracked over time including any close interactions they have. The distance versus time plot for the best match simulation is shown in Figure 8. In the genetic algorithm, the fitness is decreased by half (made worse) for any simulations where the LMC and SMC centers end up less than 15 kpc away from each other at the snapshot with the best LMC position. This prevents the best fit from getting stuck on initial conditions that result in the LMC and SMC merging before the present time.

Once the best initial positions and velocities for the MCs were determined, we also ran a simulation that had just the MW and the LMC starting at the center-of-mass (COM) of the LMC-SMC system. This is used to compare to the three-galaxy simulation to determine which LMC substructures formed as a result of interactions with the SMC.

5 RESULTS

5.1 Comparison to observations

After running ~ 8000 simulations with the genetic algorithm, we found a best match simulation and ran the same initial conditions with $10 \times$ higher resolution. A comparison between this higher-resolution best match simulation and the data is shown in Figure 9. For the rest of this section, we consider only the best match model.

For the best match simulation, when the LMC crosses $L_{\text{MS}} = 0^\circ$, the LMC position differs from the observed value by 2.8 kpc and its velocity is offset by 14.8 km s^{-1} . The SMC's position differs by 13.6 kpc and its velocity is offset by 13.2 km s^{-1} from the observed values. The largest discrepancies are the SMC's z -coordinate (offset by 12.7 kpc), the LMC's v_x (offset by 10.8 km s^{-1}), and the SMC's v_y (differs by 10.8 km s^{-1}). The fact that even after our extensive parameter space search the median MC positions and velocities are still offset by these non-negligible amounts shows the difficulty of finding the correct initial conditions.

Even with its shortcomings, the best-match simulation reproduces several observed features including the LMC ring, warp and northern arm. These will be explored in more detail below. Other features, such as the LMC hooks and the SMCNOD, are absent from the simulation.

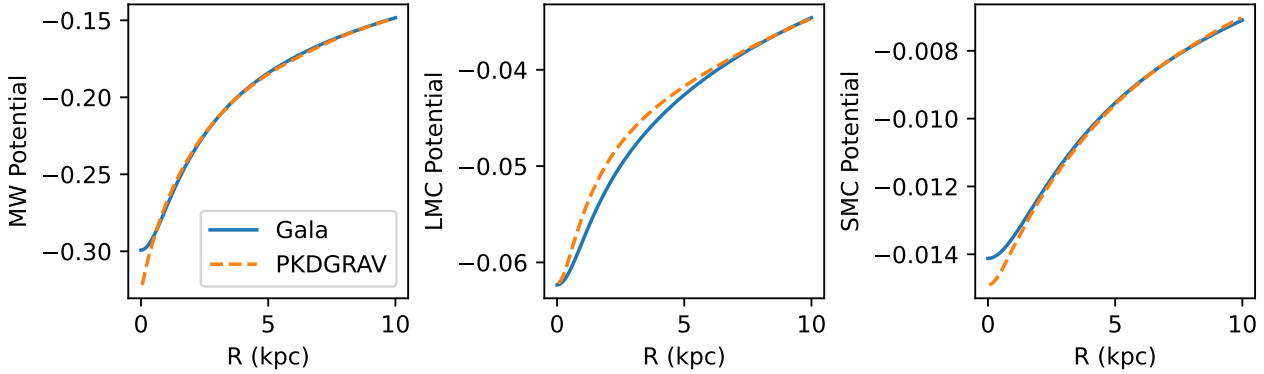


Figure 6. The potentials we use in GALA compared to the potentials of the PKDGRAV initial conditions.

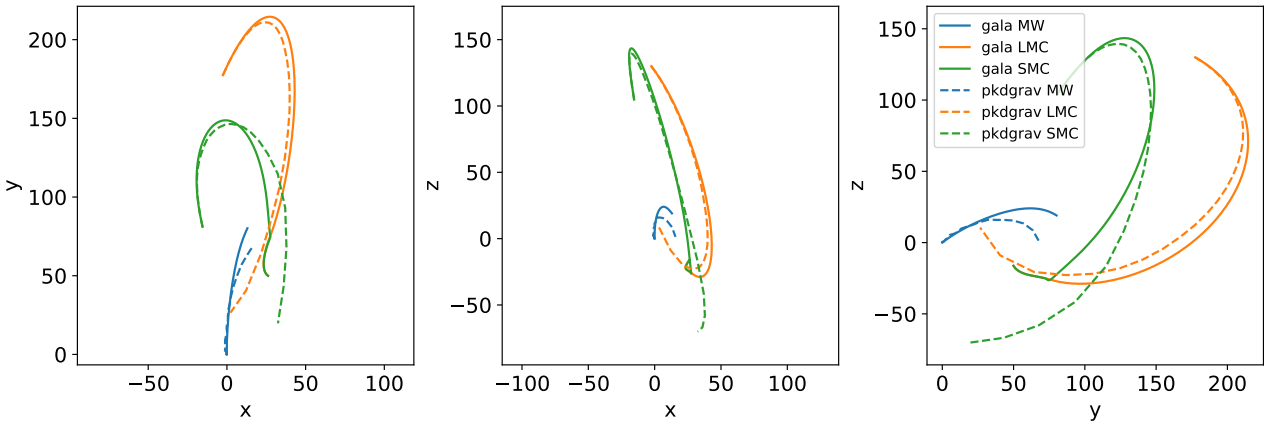


Figure 7. A comparison of orbits with GALA and PKDGRAV using the same initial conditions. The GALA orbits are shown as solid lines while the PKDGRAV orbits are dashed lines. While the orbits are fairly close at the beginning, they diverge and in the GALA run, the LMC and SMC merge. This difference could be due to the fact that with GALA, the galaxies are represented as single particles with fixed potentials, while with PKDGRAV, the shape of the galaxies and thus the shape of their potential wells can change, and stripping causes the dynamical friction and tidal forces to decrease.

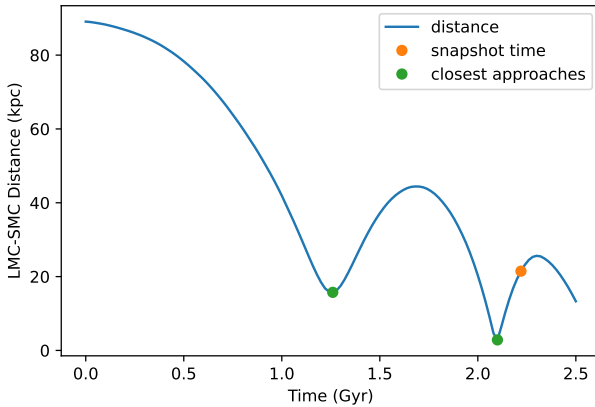


Figure 8. The distance between the LMC and SMC over time for the best match simulation. The green dots are at the closest approaches and the orange dot shows the time for the snapshot when the LMC crosses $L_{MS} = 0^\circ$.

5.2 LMC Ring

In our simulation, there is a high density ring around the center of the LMC that is similar to that described by Choi et al. (2018b) using SMASH photometry of red clump stars. The ring in the simulation

has a semi-major axis of approximately 7.5 kpc and a semi-minor axis of approximately 5 kpc, with a position angle of $\sim 30^\circ$ West of North or $\sim 150^\circ$ East of North. The observed ring has a position angle of roughly ~ 20 – 30° East of North and a semi-major axis of $\sim 7.5^\circ$ or ~ 7 kpc which is similar to what is seen in the simulation. The ring is shown in a map of the LMC in Figure 10 and the density as a function of radius for different slices of the LMC is shown in Figure 11 (similar to the right panel of Figure 1 in Choi et al. 2018b). The ring overdensity appears at radii of ~ 4 – 7 kpc depending on azimuth, as expected for an elliptical ring shape. Choi et al. (2018b) found that the overdensity was $2.5\times$ higher than the underlying exponential disc at the same radius. We find that the ring overdensity in the simulation is $\sim 2.8\times$ higher.

The origin of the ring overdensity has remained unclear and Choi et al. (2018b) postulated two main origin scenarios (1) the evolution of a one-arm spiral, and (2) collisionally-induced by a closer recent interaction with the SMC. The ring in our simulation is made up of two spiral arms. These arms first became apparent after the first interaction with the SMC, about 1 Gyr ago. After the second interaction 140 Myr ago, these two arms overlap temporarily, creating the ring-shaped overdensity. In future snapshots, the ring expands until the two spiral arms that comprise it separate. Then the current ring disappears, though another smaller ring temporarily forms at the center of the LMC. The LMC ring, therefore, can be added to

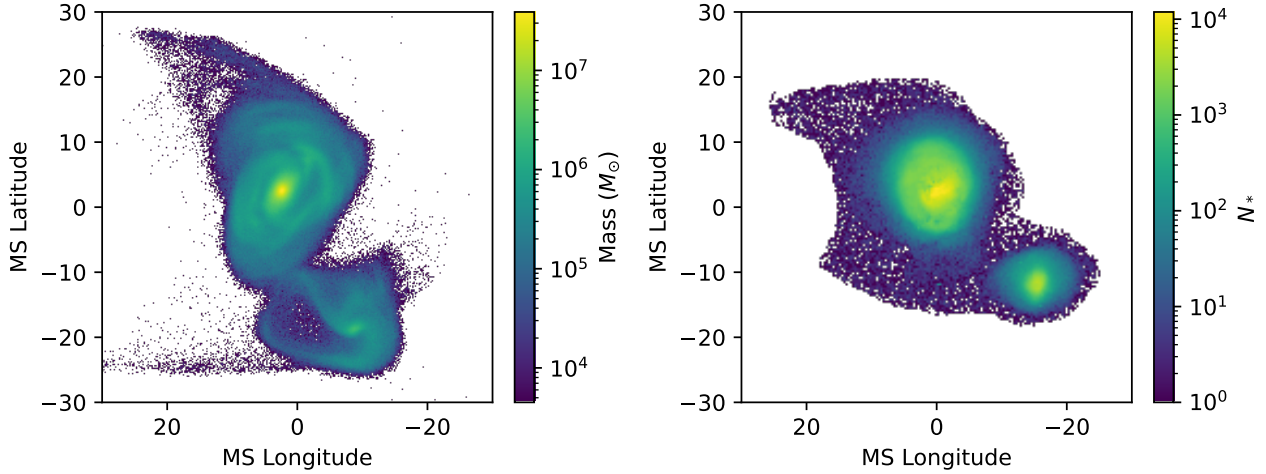


Figure 9. Comparison of density maps in MS coordinates between the best match simulation (left) and the *Gaia* data (right).

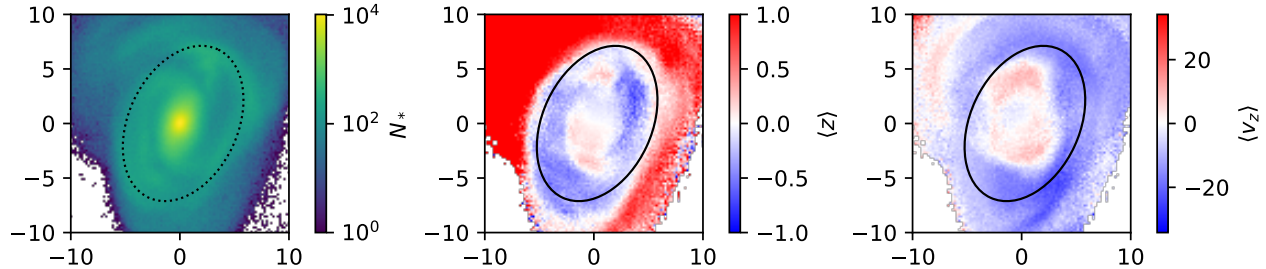


Figure 10. A face-on view of the inner LMC disc, showing the ring and colored by *left*: density, *center*: mean z , and *right*: mean V_z .

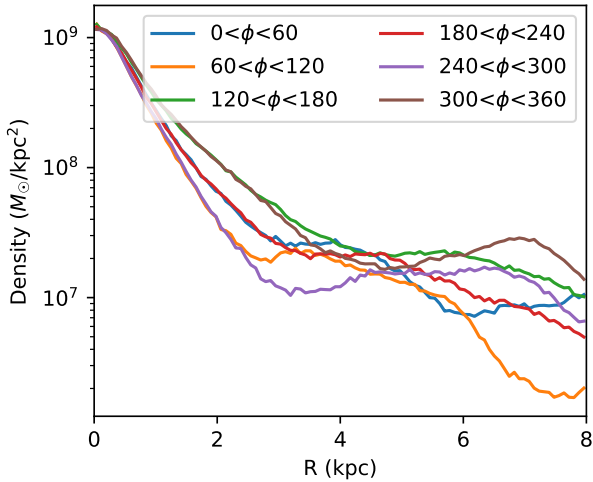


Figure 11. The mass density of the LMC disc as a function of radius in the disc plane for six slices in ϕ . The ring overdensity shows up at radii of 4–7 kpc depending on the position angle.

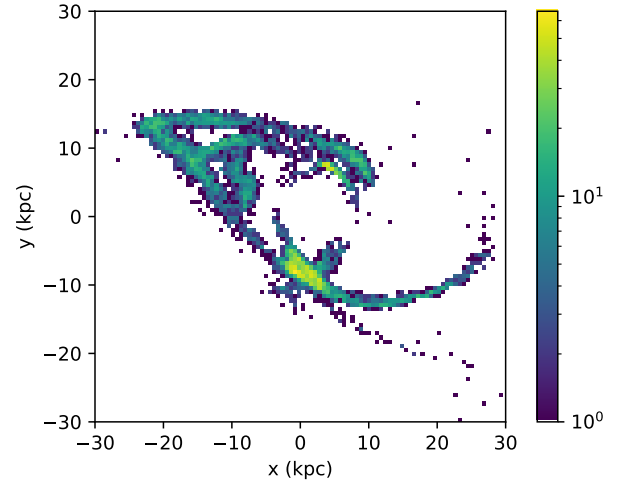


Figure 12. The face-on map of the LMC stars with a deviation value, which is determined by how the velocity components differ from the median for their radius, greater than 20.

5.3 LMC kinematic substructure

There are several signatures of LMC kinematic substructure in the simulation. To detect these substructures, we use the following procedure. The median (μ_V) and robust rms (σ_V) values of the three velocity components (V_R , V_{ϕ} , and V_z) are measured in 1 kpc radial

the mounting evidence of a recent, close encounter of the LMC and SMC.

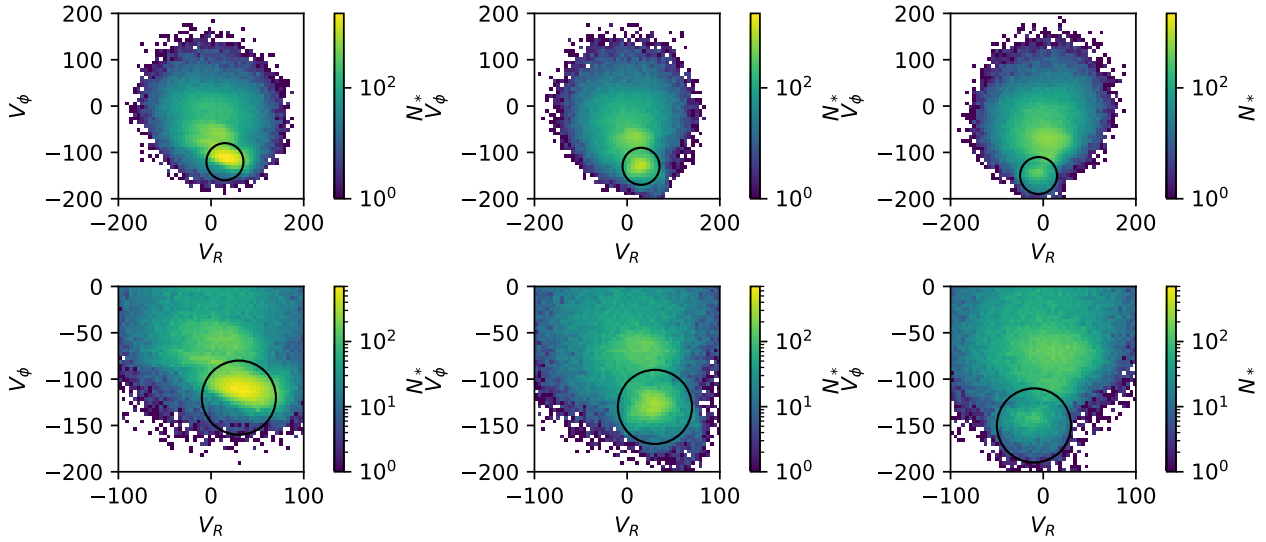


Figure 13. Plots of v_ϕ vs v_R for three different angle bins in the LMC (left: 30° – 60° , center: 60° – 90° , right: 90° – 120°). Circles show an overdensity that changes location on the plot for different angles on the LMC. The bottom row shows a zoomed in version.

bins out to a radius of 12 kpc. A ‘deviation’ value is then calculated for each star to determine how deviant its kinematics are from the bulk of the disc at its radius:

$$\text{deviation} = \sqrt{\left(\frac{V_R - \mu_{V_R}}{\sigma_{V_R}}\right)^2 + \left(\frac{V_\phi - \mu_{V_\phi}}{\sigma_{V_\phi}}\right)^2 + \left(\frac{V_z - \mu_{V_z}}{\sigma_{V_z}}\right)^2}. \quad (2)$$

Stars in the main disc following normal orbits should have small deviation values, while kinematic substructures should have larger values. The map of stars that have a deviation over 20 is shown in Figure 12.

Two distinct features are apparent in this map: (1) thin loops in the northeast, and (2) a spiral arm in the southwest that extends several kpc beyond the main disc to the west. The latter was pulled out by the SMC during their most recent interaction. This tidal arm is remarkably thin, and, therefore, also kinematically ‘cool’ with a velocity dispersion of only $\sim 25 \text{ km s}^{-1}$. Note that this feature is not visible in the map of the entire simulation in the left panel of Figure 9 because it is hidden ‘behind’ the SMC.

We employ a second technique to investigate kinematic substructure. When plotting the different cylindrical velocity components against each other for a limited azimuthal range, there is an angle-dependent overdensity at high $|v_\phi|$. Figure 13 shows this overdensity for three different eastern azimuthal slices. These two features are part of the same spiral arm as shown in Figure 14. This is also clear from looking at the different components of velocity versus angle ϕ in the LMC disc.

While there are several observed LMC substructures in the northeast that could correspond to what we see in the simulation, there is no clear observed counterpart to the western thin tidal arm. The closest possible match is the southern arm that Belokurov & Erkal (2019) suggest was tidally induced by the MW and SMC.

5.4 LMC Northern Stream

Our simulation has two arms in the northern LMC that appear in the map of kinematic features in Figure 12 and can be picked out

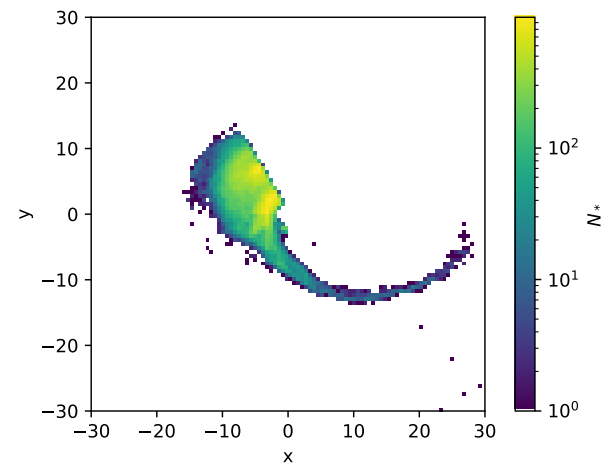


Figure 14. The combined stars of a kinematic feature of the LMC found through two different methods.

from plots of the three velocity components as a function of LMC position angle, ϕ . The northern arm begins at the northwest corner of the LMC and extends to the northeast corner. There is a stream of stars in a nearly straight line from the northeast corner past the southern part of the LMC in Figure 12 that are kinematically similar to the northern arm.

A northern stream also exists when we run the simulation without the SMC (see Figure 15), which suggests that the stream formed at least partially as a result of the interaction between the LMC and the MW. It is likely that the extra influence of the SMC enhances the northern stream.

At the western end of the northern arm, there is a ‘corner’-like feature where the arm bends at a sharp angle. This is the location where the SMC impacted the LMC during their most recent interaction. The corner does not appear in the simulation without the SMC, as shown in Figure 15.

To compare the in-plane radial velocity of our simulated northern

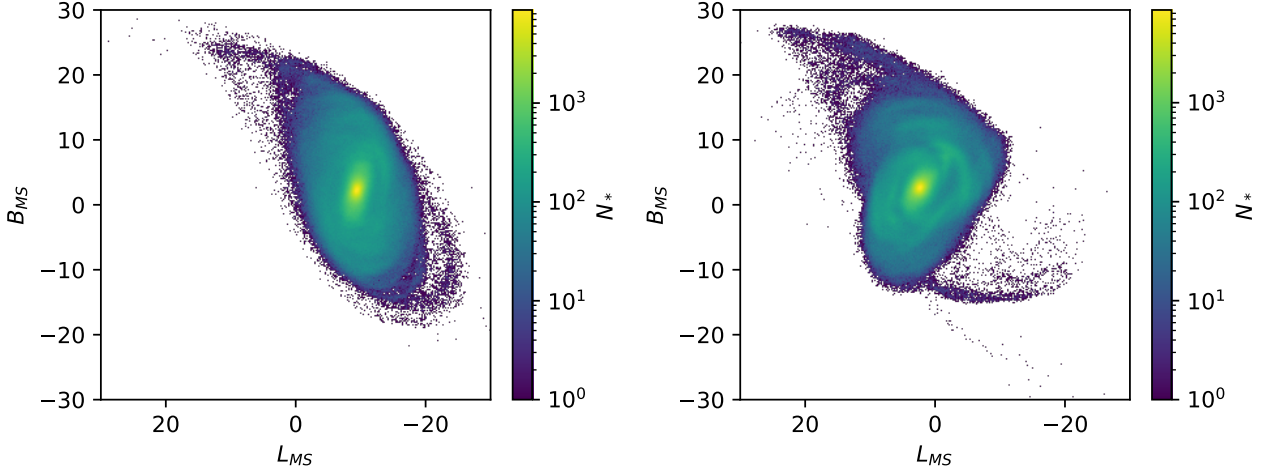


Figure 15. The LMC plotted on Magellenic Stream coordinates in simulations which exclude (left) and include (right) the SMC.

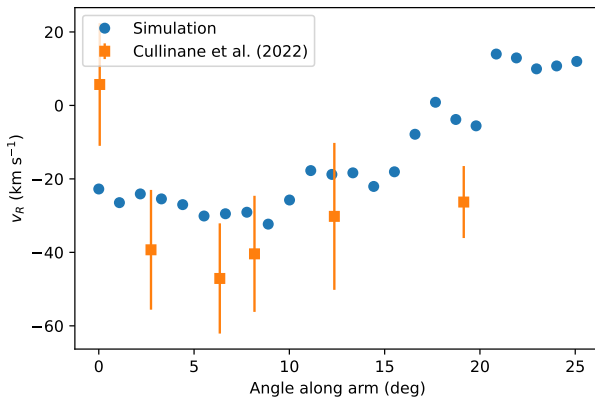


Figure 16. The in-plane radial velocity at different points along the length of our simulated northern arm compared to that measured by Cullinane et al. (2022).

arm to observations, we plot the LMC on the sky, and measure the distance in degrees along the arm from where it separates from the rest of the LMC. The comparison is shown in Figure 16. For much of the arm, the magnitude of the velocity is less than observed but the general trend of the velocity being negative and the magnitude increasing at first then decreasing gradually along the arm is similar. Toward the end of the arm in the simulation, the in-plane radial velocity crosses into positive values.

5.5 LMC disc warp and vertical oscillations

In the high resolution simulation, the LMC disc has a warp with vertical ‘ripples’ in the outskirts that appear after the most recent interaction with the SMC. At 140 Myr after the interaction, the warp in the LMC outskirts is above the disc plane (closer to the Sun), as defined by the central LMC, while at 300 Myr after the interaction the LMC warp is below the disc plane (farther from Sun). A $\langle z \rangle$ map of the LMC showing the warp and ‘ripples’ 140 Myr after the interaction is displayed in Figure 17. The ‘ripples’ (or ‘bending waves’) start in the center of the LMC and radiate outward. Figure 18 shows the $\langle z \rangle$ values versus X in a 2 kpc ‘slit’ in Y as a function of time. This clearly shows the outer disc oscillating vertically with time. Roughly

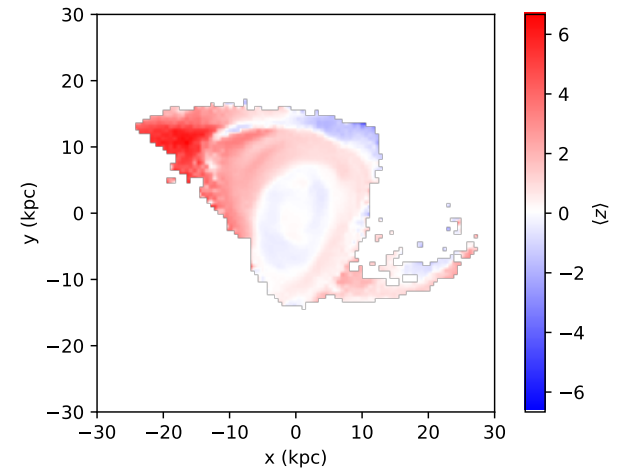


Figure 17. Face-on map of the LMC colored by mean z , showing the ‘ripples’ in the disc.

half of a vertical oscillation occurs in 300 Myr indicating the period is ~ 600 Myr.

Choi et al. (2018a) detected a southwestern warp in the LMC at a radius of 7° and extending to 4 kpc below the LMC midplane. Later, Saroona & Subramanian (2022) detected the northern component of the warp (towards the northeast) at a radius of 7° and extending 1.2 kpc below the LMC midplane, in the same direction of the southern warp. Tidal interactions generally create S-shaped warps (e.g., Toomre & Toomre 1972), therefore, the detected U-shaped warp was somewhat unexpected. However, the U-shaped warp could be an effect of the bending waves that we detect in our simulation that are produced in a direct collision of the LMC and SMC. The strong oscillations start around a radius of 7–8 kpc in the simulation which is at a similar radius to the observed warps.

5.6 SMC Expansion and Rotation

In our Model A high-resolution simulation, the SMC radially expands after the most recent interaction with the LMC. The outward radial velocity of the stars increases with radius, as can be seen in the v_R

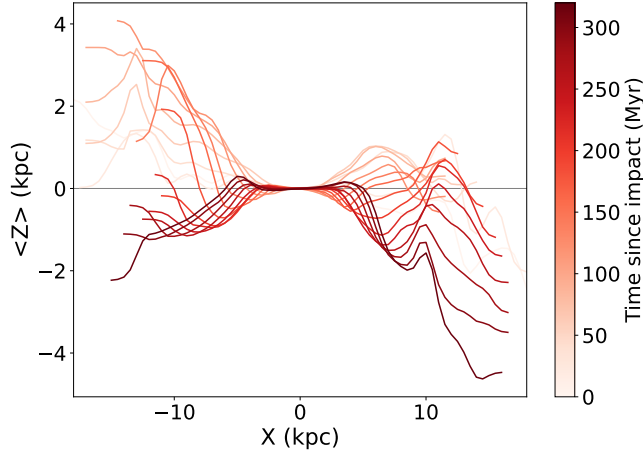


Figure 18. Vertical oscillations in the LMC disc. Mean z values versus X in a narrow 2 kpc Y-slit for the 340 Myr after the most recent LMC-SMC collision. The vertical oscillations are clearly seen in both panels.

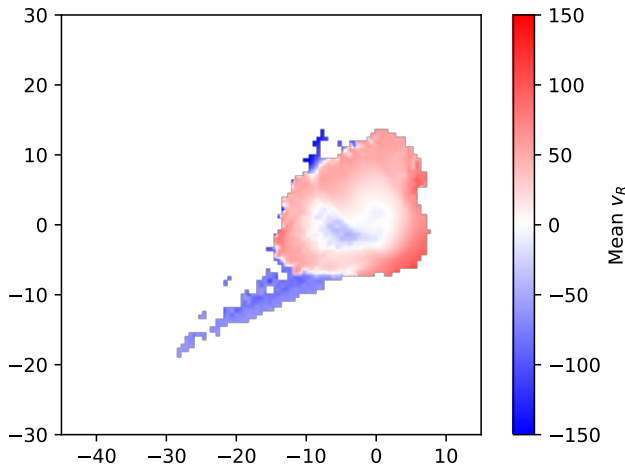


Figure 19. Face-on map of the SMC colored by mean v_R .

map (Figure 19), while the linear radial dependence can be seen more clearly in the left panel of Figure 20. We find that the slope of v_R as a function of R to be $9.86 \text{ km s}^{-1} \text{ kpc}^{-1}$ extending to a radius of 6 kpc. The kinematic analysis of Zivick et al. (2021) of the SMC *Gaia* DR2 proper motions (to a radius of $\sim 4.5^\circ$) found a tidal expansion term of $10 \pm 1 \text{ km s}^{-1} \text{ kpc}^{-1}$ in the direction of the LMC. Figure 21 shows the tidal expansion of the SMC in the direction of the LMC in our simulation. The Zivick et al. result is indicated by a blue line indicating a good overall agreement.

Before the LMC-SMC close interactions, the SMC’s rotation velocity is 60.5 km s^{-1} and reaches a maximum at a radius of ~ 3 kpc in our simulation. After the most recent LMC-SMC impact, the SMC’s rotation is diminished, but there remains a clear ‘leftover’ rotation in the simulation. The rotation velocity increases with radius until it reaches a maximum of $\sim 38 \text{ km s}^{-1}$ at a radius of ~ 6 kpc (right panel of Figure 20). For stars at a radius around 1 kpc, the median is about 18 km s^{-1} . This is within the range of $15\text{--}25 \text{ km s}^{-1}$ for rotation at 1 kpc found by Zivick et al. (2021). The Zivick et al. kinematic analysis determined a maximum rotation velocity of 20 km s^{-1} reaching

the maximum at 1 kpc. This is lower than the value we find in the simulation. The v/σ for the SMC remains fairly constant at ~ 3.5 before the first interaction, at which point it drops to ~ 2.5 . At the most recent interaction at 2.06 Gyr, it drops again to ~ 1.0 and continues to decrease sharply from there. In the ‘current’ snapshot, $v/\sigma = 0.79$. This is slightly more than the observed value of $v/\sigma \leq 0.6$ (Harris & Zaritsky 2006), but it reaches this value about 60 Myr after the ‘current’ snapshot.

5.7 SMC Kinematic Substructure

In the SMC, there is a substructure that can be seen in the plot of v_R vs. R , shown in Figure 22. As shown in Figure 23, the stars below the cut in Figure 22 are mostly in two arms that start near the center and extend out to a larger radius than the main SMC. The stars in the arm to the south were pulled away from the SMC during the collision with the LMC, while the one to the east mostly remains within the SMC disc. The stars in the southern arm have a similar velocity in the x direction ($\sim 110 \text{ km s}^{-1}$) and in the simulation continue past the main SMC after the current snapshot. While there is observed stellar substructure called the SMC Southern Overdensity (SMCSOD; Massana et al. 2024) it is as of yet unclear if these are the same structures. This feature in our simulation does not appear to be kinematically similar to the observed SMCSOD. The stars in the observed SMCSOD tend have a proper motion μ_B equal to or greater than the main SMC (Massana et al. 2024), while the μ_B for the stars in the simulated feature is lower than for the main SMC.

5.8 SMC Stellar Radial Density Profile

The simulated SMC disc density can be modeled as two exponentials out to a radius of 5.5 kpc, one with scale length 0.46 kpc and the other with scale length 7.87 kpc. The first models the central SMC ‘core’, while the second accounts for the more extended main body and tidal arms. At larger radii, the density of the SMC breaks and drops off after 5.5 kpc, as shown in Figure 24. This drop in density is likely not due to the truncation of the SMC disk, since the overdensity is moving outward from the center of the SMC at the time of this snapshot. We compare the simulation profile to the *Gaia* SMC red giant branch starcount data (right panel of Figure 24), which show that the SMC can be modeled fairly well with a single exponential profile for most of its extent, with a slight overdensity at a radius of $\sim 4\text{--}5$ kpc. Observations show the SMC has a more elliptically-shaped core in the inner $1\text{--}2^\circ$ but is more circularly shaped at larger radii (Gaia Collaboration et al. 2021b). These could correspond to the two components seen in the simulation. In the periphery, Nidever et al. (2011) and Pieres et al. (2017) both found extended SMC stellar components beyond $\sim 7^\circ$ which in the north corresponds to the SMCNOD. There is no clear counterpart to the SMCNOD in our simulation.

5.9 SMC Distance Bimodality

The SMC exhibits a distance bimodality in the east, towards the direction of the LMC, which is clearly seen in the CMD distribution of red clump stars (e.g., Hatzidimitriou & Hawkins 1989; Nidever et al. 2013). The nearer group of stars, which are ~ 10 kpc closer to the Sun than the main SMC, were likely separated from the SMC by tidal interactions with the LMC (Almeida et al. 2024). With the simulated SMC, we divide the SMC into a spatial 5×5 grid (see Figure 25) and show their distance distributions in Figure 26. The region where the

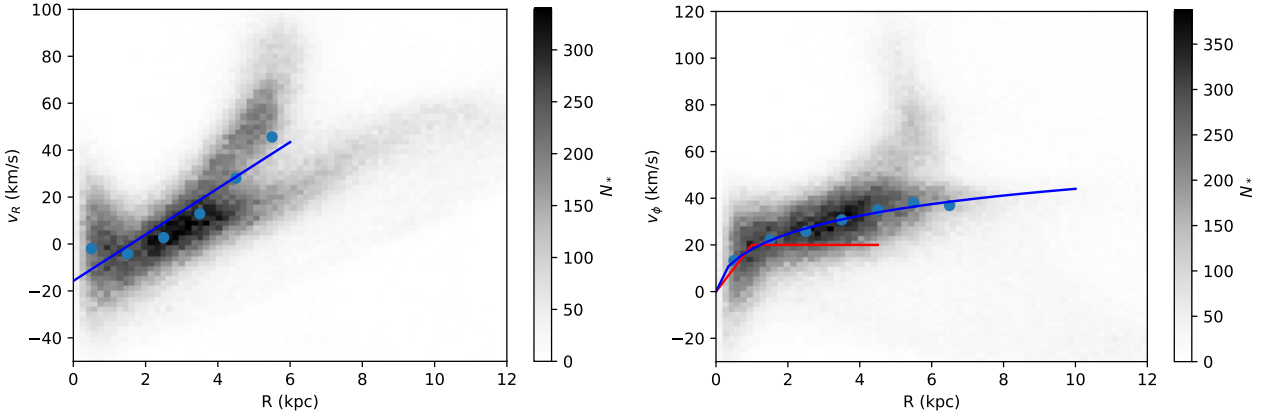


Figure 20. Kinematics of SMC star particles. (Left) v_R versus R . The filled circles show the median velocity value for each of the first six 1 kpc radial bins. A linear fit of $9.86 \text{ km s}^{-1} \text{ kpc}^{-1}$ is shown by the blue line. (Right) v_ϕ vs R . The median for each 1 kpc radial bin is again shown. A rotation curve matching the median values is shown in blue. The Zivick et al. (2021) results are in red.

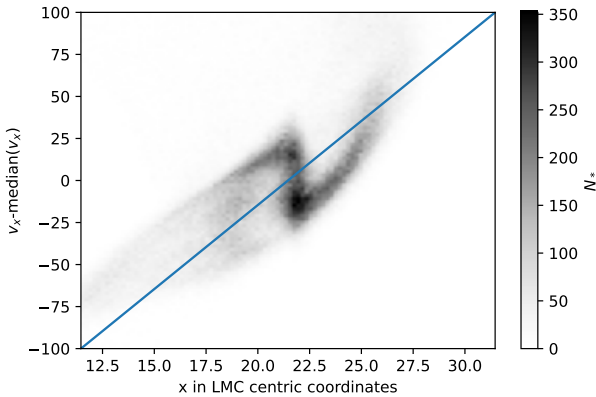


Figure 21. The tidal expansion of the SMC. The coordinate system here is centered on the LMC and the SMC is on the x-axis, so v_x is the component of the SMC's velocity toward or away from the LMC (negative is towards the LMC). The blue line shows the tidal expansion of $10 \text{ km s}^{-1} \text{ kpc}^{-1}$ found by Zivick et al. (2021).

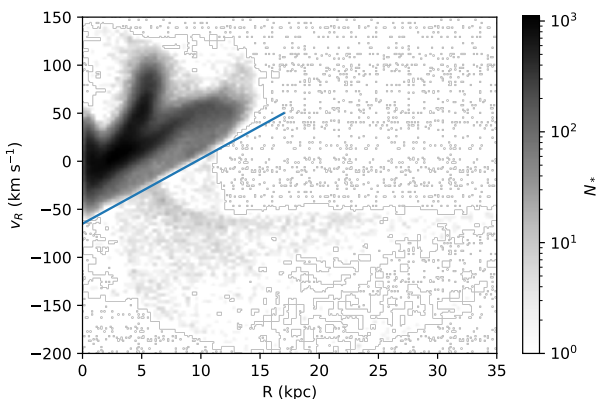


Figure 22. SMC v_R vs. R with different axis limits than Figure 20 to show stars with higher radii and negative v_R . The blue line is at the cutoff between the main SMC disc and a kinematic feature.

distance bimodality is observed lies at the top of the figures at higher B_{MS} . The central and western (bottom panels) regions show a fairly narrow single-peaked distance profile consistent with observations, while the eastern regions exhibit a clear bimodality resembling that observed. The bimodality appears after the most recent interaction between the MCs.

The eastern SMC is composed of two components. These are easily separated in azimuthal velocity in the SMC-centric frame into a prograde and retrograde component. Figure 27 shows the spatial density of all stars and the two components in the top panels, while distance vs. B_{MS} is shown in the bottom panels. The prograde component is more distant and has a spiral arm-like shape. In contrast, the retrograde component is closer and has the shape of a tidal arm extending from the central SMC. In addition, the stars that make up the retrograde component all come from the inner SMC ($R < 5 \text{ kpc}$). This is consistent with the results of Almeida et al. (2024) who found that the closer SMC component is tidally stripped from the inner SMC.

5.10 Multiple LMC Initial Conditions

We also ran the simulation with the same starting positions and velocities but with different LMC models as described in section 3. The maps of the different models at the ‘current’ snapshot are shown in Figure 28. In all models, there are two interactions between the MCs that occur at about the same times. Every model also ends up with a northern stream, two arms forming a high density ring in the LMC disc, and an arm pulled out from the LMC like the feature described in subsection 5.3. Therefore, we conclude that these are robust features of the models.

Other things, such as the time at which the LMC crosses the MS longitude zero and the position of the SMC, differ between models. In both models where we change the thickness of the LMC disc (B and C) as well as the one with a more diffuse dark matter halo (G), the LMC crosses MS longitude zero earlier than in the fiducial simulation. The time difference is 20 Myr in model C, 40 Myr in model G, and 80 Myr in model B. Since the timing of when the LMC crosses $L_{\text{MS}} = 0$ is how we define the ‘current’ snapshot, it might be significant to our other results that these simulations did not run as long as the others, which had the LMC cross zero at the same time as for model A. In two of these simulations (models B and G), the location of the SMC is more directly south of the LMC than for other

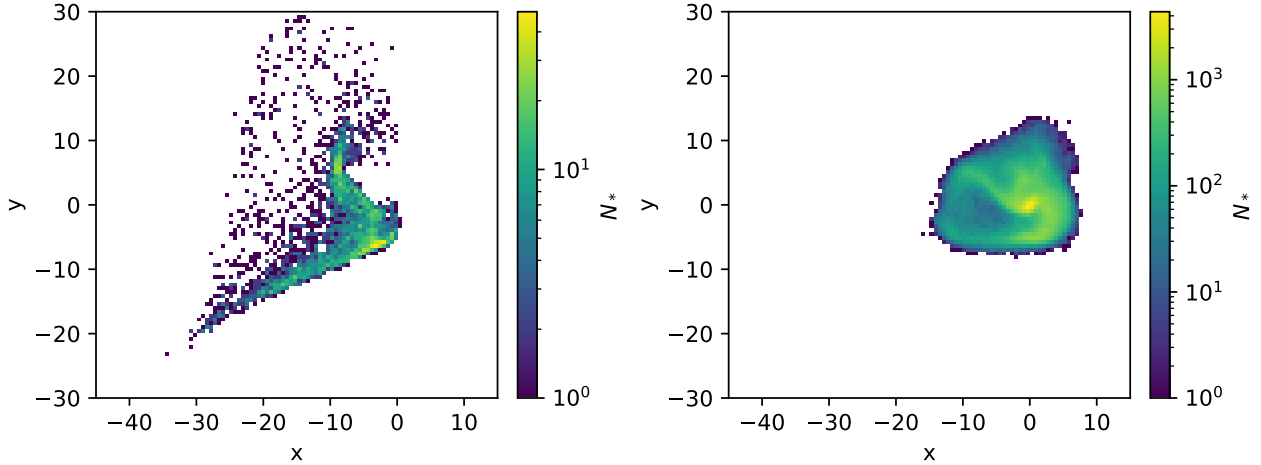


Figure 23. The face-on SMC in the SMC-centric coordinate system. *Left:* The stars below the cut in Figure 22. *Right:* The stars above that cut.

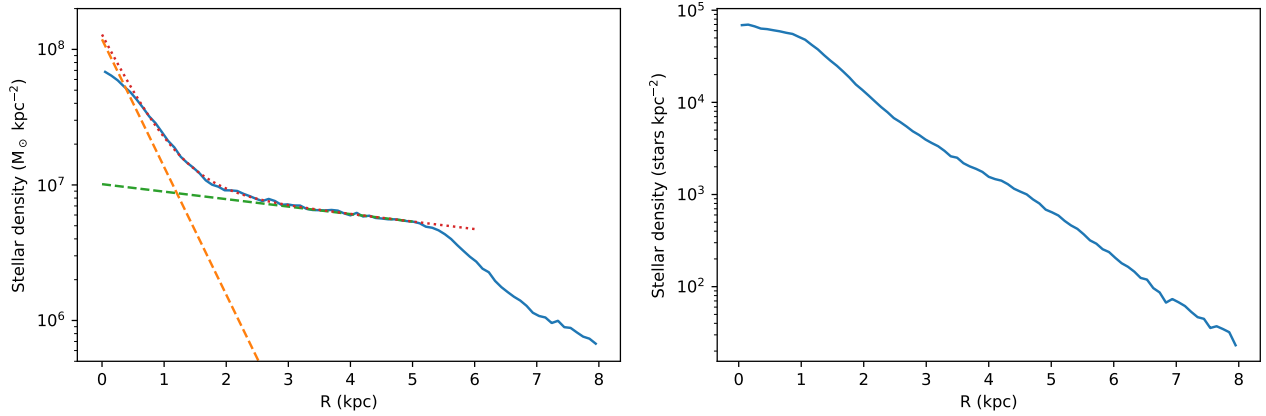


Figure 24. The radial density of the SMC (*left*) in the simulation with two exponential discs (dashed lines) and their sum (dotted line) (*right*) from *Gaia* data.

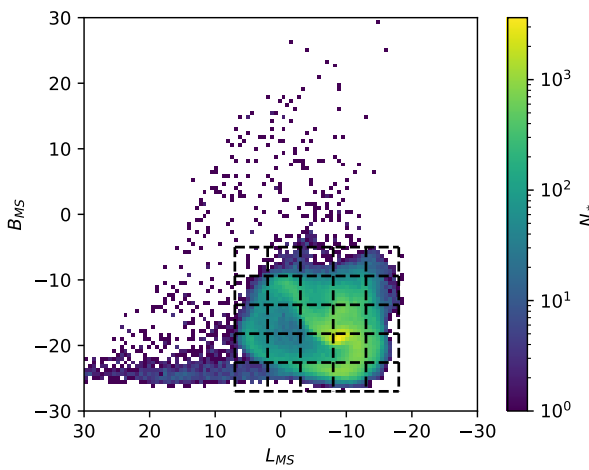


Figure 25. Map of simulated SMC stars on Magellanic Stream coordinates with dashed lines dividing the SMC into different regions.

models. The SMC is also in a similar location south of the LMC in model F. In the others, the SMC is in a similar location in the sky as for the fiducial simulation.

The direction and amplitude of the warp at the ‘current’ time differ substantially across the models. Models A, C, and D all exhibit a positive warp (toward the Sun), with model D evolving in a way that closely mirrors model A. In contrast, models B and G have a negative warp (away from the Sun). Model F shows no coherent warp in either direction; instead, it develops only small-scale ripples. The radial extent of these ripples also varies with disc thickness. In model B, which uses the thicker disc, the ripples appear only in the outer LMC (beyond ~ 8 kpc). In model C, with the thinner disc, they begin much farther in, at roughly 5 kpc. Finally, the LMC disc for model G bends in both directions at different azimuths rather than forming a uniform, global warp.

Overall, the parameter that had the most effect on the simulation when changed was the concentration of the dark matter halo. The range of parameter values we looked at left much uncertainty in the characteristics of the LMC.

6 DISCUSSION

While it is possible to ‘successfully’ reproduce observational results with simulations, such as the Sagittarius stellar stream by Law & Majewski (2010) and the M31 great southern stream by

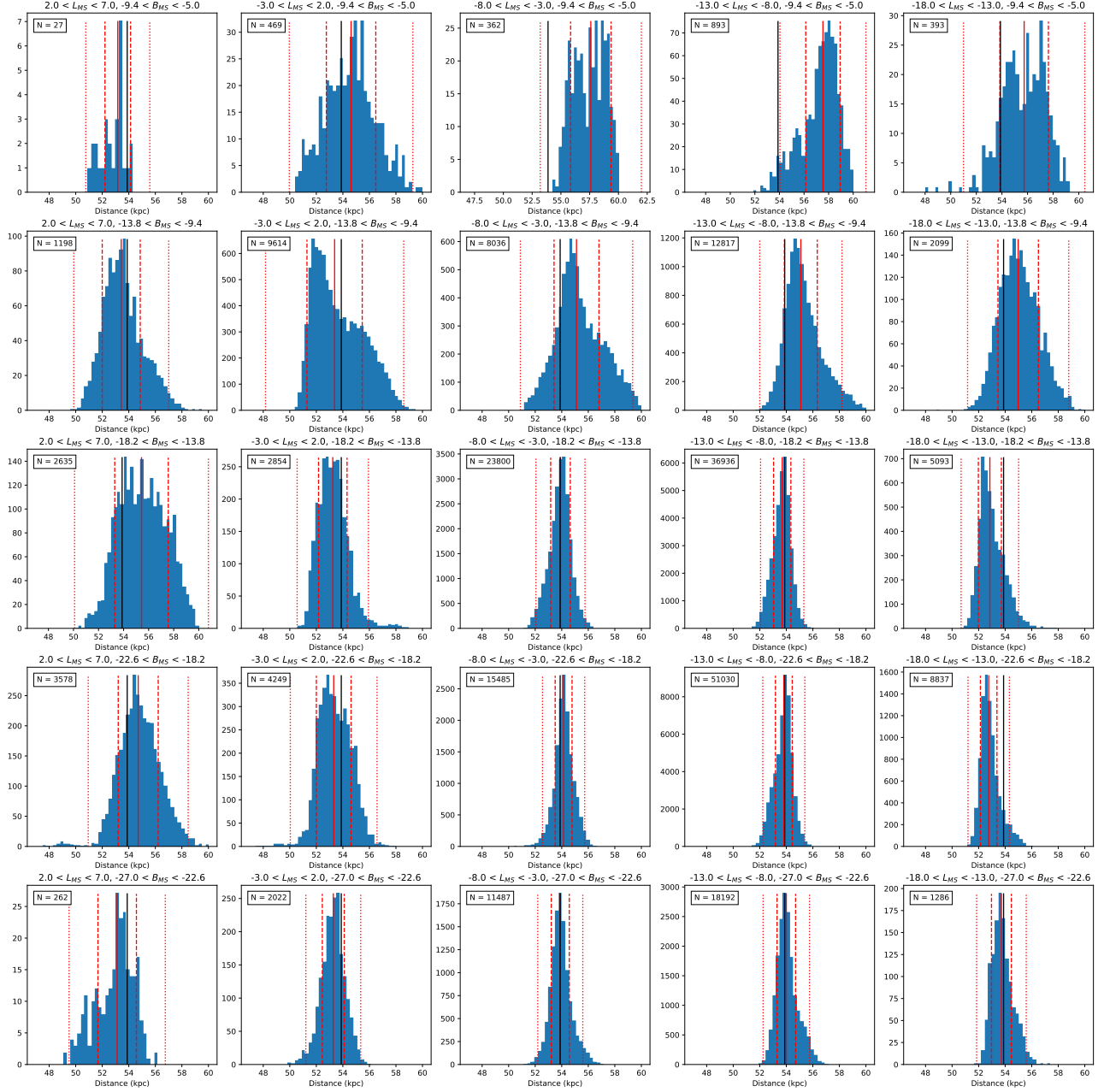


Figure 26. Histograms of distances to simulated SMC stars. Each histogram is of stars in the box in the same grid location as in Figure 25. The solid red line is the median distance, the dashed lines are one median absolute deviation (MAD) away from the median, and the dotted lines are 2.5 MADs away from the median. The black line is the median distance of all the SMC stars.

Fardal et al. (2013), it is generally challenging to match simulations to data. One exception is the Made-to-Measure technique (Syer & Tremaine 1996), which fits a system to observations by varying particle weights within a prescribed potential — an approach distinct from fully self-consistent N-body simulations and less suited to strongly non-equilibrium systems like the Magellanic Clouds. The Magellanic System is notoriously difficult to model due to the multiple strong interactions and the complexity of the system. Even with more than 8000 simulations, our genetic algorithm search of the parameter space found an approximate match to the central MC positions and velocities. Even so, there are a number of observational stellar features that are reproduced in our best-match simulation.

The LMC ring identified and characterized by Choi et al. (2018b)

is clearly reproduced in our simulation. While the origin of the ring remained unclear, we find that it is collisionally-induced by the recent direct SMC-LMC collision. The ring is made up of two overlapping arms in the LMC, and most of the stars in the ring are moving outward with a median v_R of 12.7 km s^{-1} . This ring is present in all the simulations we ran with different LMC parameters, so it is robust.

In addition, our simulation reproduces the northern LMC stream which is a prominent observational substructure in the LMC outskirts. While Belokurov & Erkal (2019) were able to generate a northern stream with a simulation of only the LMC and MW, we find that the presence of the SMC significantly enhances the northern stream and modifies its shape. The northwestern edge of the stream

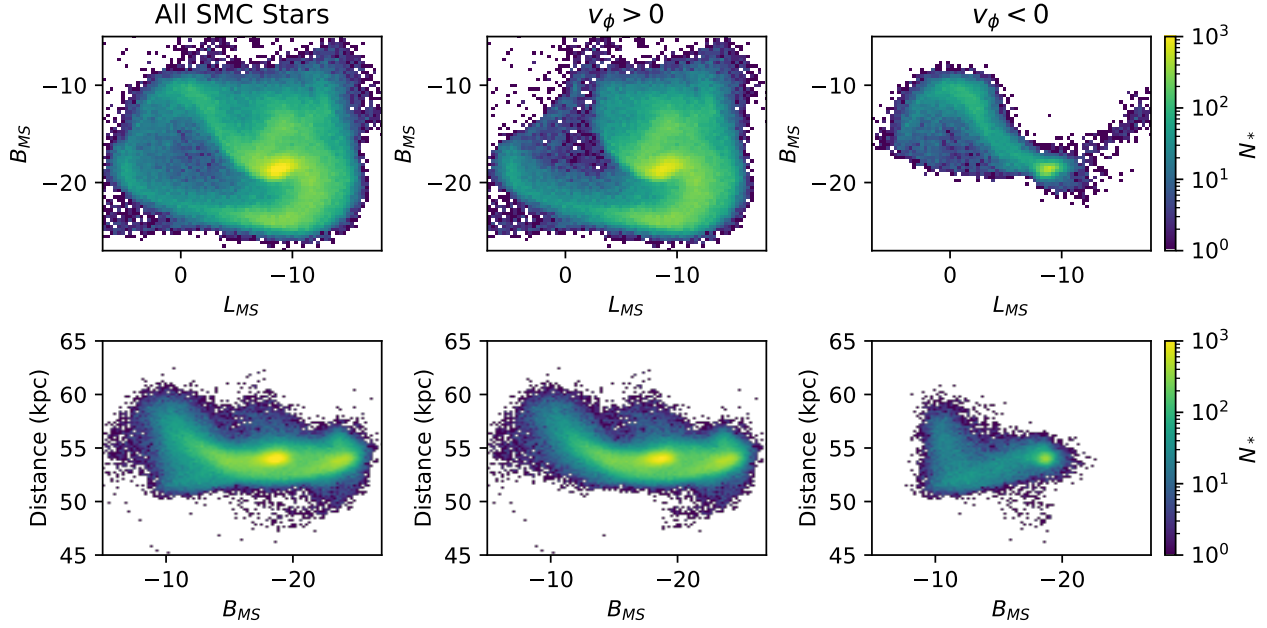


Figure 27. Density map on the sky and distance vs. B_{MS} for simulated SMC stars. The left panels include all SMC stars, the center panels include only the stars where $v_\phi > 0$, and the right panels include only the stars where $v_\phi < 0$.

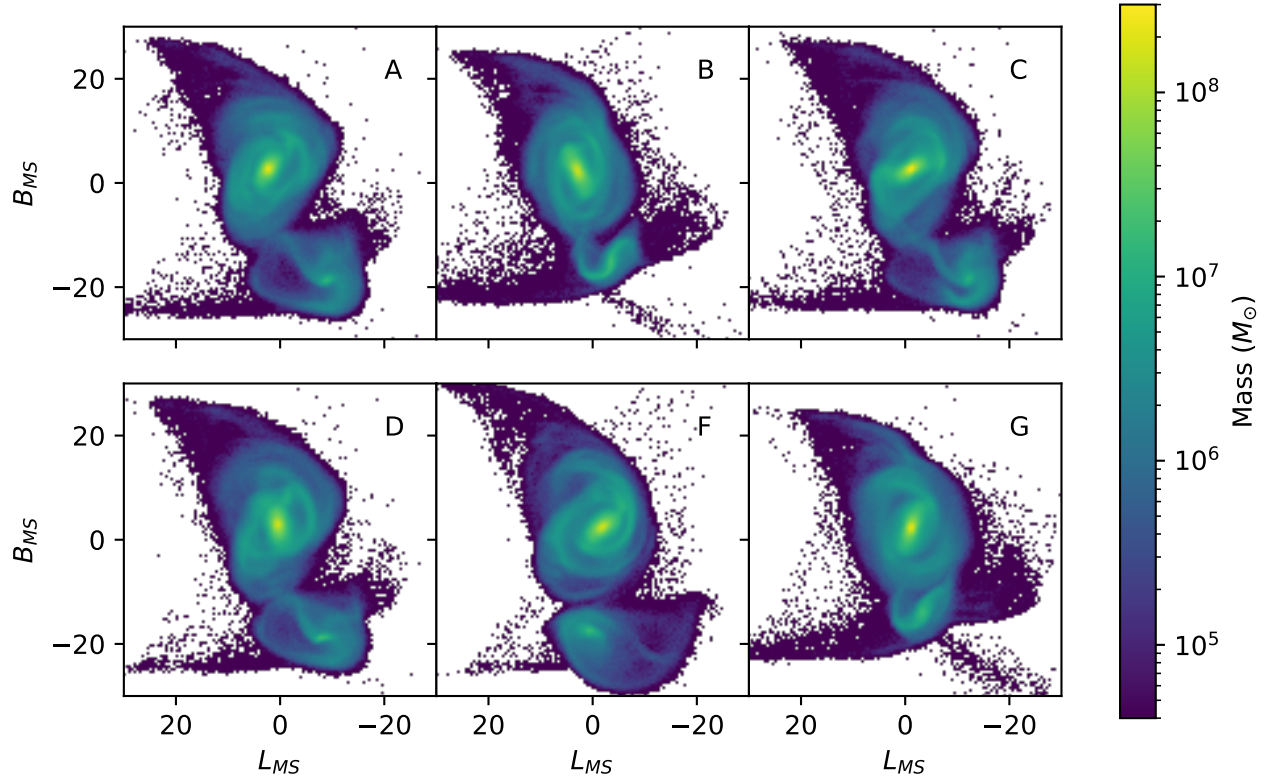


Figure 28. The maps of the different simulations at the ‘current’ snapshot for each model. *Top row:* models A, B, and C. *Bottom row:* models D, F, and G.

becomes substantially kinked and the western edge of the LMC disc quite linear similar to what is observed.

The recent direct collision of the LMC and SMC also substantially affected the structure and kinematics of the SMC. The simulated SMC stars have a significant positive radial velocity component especially beyond a radius of ~ 2 kpc. This is similar to the tidal expansion observed by Zivick et al. (2018). Even with the dramatic disturbance to the SMC’s structure, it shows residual rotation – although at levels $\sim 2\times$ that seen by Zivick et al. in the *Gaia* data.

The most pronounced SMC substructure is the distance bimodality on the eastern side. This is also found in our simulation where the eastern side of the SMC is composed of two components. The pro-grade component is more distant and part of the main SMC structure, whereas the retrograde component is closer and tidally pulled from the SMC center. This confirms the findings of Almeida et al. (2024) which showed that the metallicity distribution function of the closer eastern component is very similar to the central SMC, while the more distant eastern component is like the western SMC periphery.

A striking phenomenon in our high resolution interaction simulation is the vertical oscillations of the outer LMC disc. This is a direct result of the recent collision of the two galaxies. These oscillations appear in most of the simulations where we vary LMC parameters, but are less pronounced in the one with more concentrated dark matter halo. While similar vertical oscillations have been observed in the Milky Way, which could be due to the influence of Sagittarius dwarf spheroidal and likely the LMC (e.g., Gómez et al. 2016; Laporte et al. 2018), such oscillations have not yet been detected in the LMC. We predict that such vertical oscillations should be observable in the LMC, especially at larger radii, if the LMC and SMC had a direct collision. The U-shaped warp detected by Choi et al. (2018a) and Saroona & Subramanian (2022) could be the inner edge of the vertical oscillations. We note that Oden et al. (2025) recently discovered that the warp is indeed U-shaped and extends to a radius of ~ 15 kpc.

Our simulation does not reproduce the LMC southern hooks or the SMCNOD feature. It is quite possible that these were created by interactions of the MCs before 2.5 Gyr ago. In future work, we plan to start the simulations at earlier times to capture some of these events.

7 CONCLUSIONS

We use a suite of N-body simulations of the LMC, SMC and MW system to reproduce observed stellar features in the Magellanic System. Using a genetic algorithm, we ran over 8000 simulations of the three galaxies until we found initial conditions that resulted in the MCs being close to their observed locations after two close interactions in the past 2.5 Gyr.

Our main findings are as follows:

- There are two close passages between the MCs in the past 2.5 Gyr. In our best simulation, they are about 940 Myr and 140 Myr before the LMC reaches its current position.
- The simulation reproduces the observed LMC ring which is a temporary structure of two collisionally-induced LMC spiral arms by the recent close SMC-LMC collision which are moving radially outward.
- The LMC northern stream is reproduced by a combination of MW and SMC tidal forces on the LMC. The influence of the SMC enhances the feature and creates a unique kinked shape similar to what is observed.
- The simulated SMC exhibits radial expansion after the recent

collision which is similar to the observed tidal expansion. In addition, there is residual rotation as also observed, but at a level $\sim 2\times$ higher.

- The observed distance bimodality in the eastern SMC is reproduced. This is due to two eastern components, one of which is a retrograde tidal arm pulled from the central SMC and more nearby. This is consistent with recent observations of SMC abundances.
- Kinematic substructures are observed in both the LMC and SMC that do not have any clear observational counterparts.
- The warp in the outer LMC shows pronounced vertical oscillations from the last SMC encounter. The U-shaped warp is consistent with observational results of the southern and northern warps in the LMC periphery.
- Changing the thickness of the LMC disc affects the size and direction of the warp. In our simulation with the higher density LMC halo, only a small warp appears, while in the one with the lower density halo, the warp is S-shaped rather than U-shaped.

ACKNOWLEDGEMENTS

B.R.G. and D.L.N. acknowledge support from National Science Foundation grants AST 1908331 and 2408159.

Computational efforts were performed on the Tempest High Performance Computing System, operated and supported by University Information Technology Research Cyberinfrastructure (RRID:SCR_026229) at Montana State University. Some simulations were also run on the Flatiron Institute’s Rusty computing cluster, which is supported by the Simon’s Foundation. Additional early simulations were run at the High Performance Computer Facility of the University of Lancashire.

Portions of the text were refined with the assistance of OpenAI’s ChatGPT (GPT-5), which was used to improve clarity, grammar, and style.

DATA AVAILABILITY

Our fiducial simulation is available at <https://doi.org/10.5061/dryad.1vhhmgr82>

REFERENCES

- Abdurro’uf et al., 2022, *ApJS*, **259**, 35
 Almeida A., et al., 2024, *MNRAS*, **529**, 3858
 Andrae R., Rix H.-W., Chandra V., 2023, *ApJS*, **267**, 8
 Barger K. A., Haffner L. M., Bland-Hawthorn J., 2013, *ApJ*, **771**, 132
 Belokurov V. A., Erkal D., 2019, *MNRAS*, **482**, L9
 Besla G., 2015, *arXiv e-prints*, p. [arXiv:1511.03346](https://arxiv.org/abs/1511.03346)
 Besla G., Kallivayalil N., Hernquist L., Robertson B., Cox T. J., van der Marel R. P., Alcock C., 2007, *ApJ*, **668**, 949
 Besla G., Kallivayalil N., Hernquist L., van der Marel R. P., Cox T. J., Kereš D., 2012, *MNRAS*, **421**, 2109
 Binney J., Tremaine S., 2008, *Galactic Dynamics: Second Edition*
 Brüns C., et al., 2005, *A&A*, **432**, 45
 Carrera R., Gallart C., Hardy E., Aparicio A., Zinn R., 2008, *AJ*, **135**, 836
 Chandra V., et al., 2023, *ApJ*, **956**, 110
 Choi Y., et al., 2018a, *ApJ*, **866**, 90
 Choi Y., et al., 2018b, *ApJ*, **869**, 2
 Choi Y., Olsen K. A. G., Besla G., van der Marel R. P., Zivick P., Kallivayalil N., Nidever D. L., 2022, *ApJ*, **927**, 153
 Connors T. W., Kawata D., Gibson B. K., 2006, *MNRAS*, **371**, 108
 Cullinane L. R., Mackey A. D., Da Costa G. S., Erkal D., Koposov S. E., Belokurov V., 2022, *MNRAS*, **510**, 445
 Dark Energy Survey Collaboration et al., 2016, *MNRAS*, **460**, 1270

- Diaz J. D., Bekki K., 2012, *ApJ*, **750**, 36
- Erkal D., et al., 2019, *MNRAS*, p. 1318
- Fardal M. A., et al., 2013, *MNRAS*, **434**, 2779
- Filipovic M. D., et al., 1998, *A&AS*, **127**, 119
- Gaia Collaboration et al., 2021a, *A&A*, **649**, A1
- Gaia Collaboration et al., 2021b, *A&A*, **649**, A7
- Gómez F. A., White S. D. M., Marinacci F., Slater C. T., Grand R. J. J., Springel V., Pakmor R., 2016, *MNRAS*, **456**, 2779
- Hagen L. M. Z., Siegel M. H., Hoversten E. A., Gronwall C., Immler S., Hagen A., 2017, *MNRAS*, **466**, 4540
- Harris J., Zaritsky D., 2006, *AJ*, **131**, 2514
- Hatzidimitriou D., Hawkins M. R. S., 1989, *MNRAS*, **241**, 667
- Jiménez-Arranz Ó., Roca-Fàbregas S., Romero-Gómez M., Luri X., Bernet M., McMillan P. J., Chemin L., 2024, *A&A*, **688**, A51
- Kallivayalil N., van der Marel R. P., Besla G., Anderson J., Alcock C., 2013, *ApJ*, **764**, 161
- Klein U., Haynes R. F., Wielebinski R., Meinert D., 1993, *A&A*, **271**, 402
- Kunkel W. E., 1979, *ApJ*, **228**, 718
- Laporte C. F. P., Johnston K. V., Gómez F. A., Garavito-Camargo N., Besla G., 2018, *MNRAS*, **481**, 286
- Law D. R., Majewski S. R., 2010, *ApJ*, **714**, 229
- Lin D. N. C., Lynden-Bell D., 1977, *MNRAS*, **181**, 59
- Lucchini S., D'Onghia E., Fox A. J., Bustard C., Bland-Hawthorn J., Zweibel E., 2020, *Nature*, **585**, 203
- Lucchini S., D'Onghia E., Fox A. J., 2021, *ApJ*, **921**, L36
- Lucchini S., D'Onghia E., Fox A. J., 2024, *ApJ*, **967**, 16
- Mackey A. D., Koposov S. E., Erkal D., Belokurov V., Da Costa G. S., Gómez F. A., 2016, *MNRAS*, **459**, 239
- Mackey D., Koposov S., Da Costa G., Belokurov V., Erkal D., Kuzma P., 2018, *ApJ*, **858**, L21
- Majewski S. R., Nidever D. L., Muñoz R. R., Patterson R. J., Kunkel W. E., Carlin J. L., 2009, in Van Loon J. T., Oliveira J. M., eds, IAU Symposium Vol. 256, The Magellanic System: Stars, Gas, and Galaxies. pp 51–56, doi:10.1017/S1743921308028251
- Majewski S. R., et al., 2017, *AJ*, **154**, 94
- Massana P., Nidever D. L., Olsen K., 2024, *MNRAS*, **527**, 8706
- Murai T., Fujimoto M., 1980, *PASJ*, **32**, 581
- Nidever D. L., Majewski S. R., Butler Burton W., 2008, *ApJ*, **679**, 432
- Nidever D. L., Majewski S. R., Muñoz R. R., Beaton R. L., Patterson R. J., Kunkel W. E., 2011, *ApJ*, **733**, L10
- Nidever D. L., Monachesi A., Bell E. F., Majewski S. R., Muñoz R. R., Beaton R. L., 2013, *ApJ*, **779**, 145
- Nidever D. L., et al., 2017, *AJ*, **154**, 199
- Nidever D. L., et al., 2019a, *ApJ*, **874**, 118
- Nidever D. L., et al., 2019b, *ApJ*, **887**, 115
- Nidever D. L., et al., 2020, *ApJ*, **895**, 88
- Nidever D. L., et al., 2021, *AJ*, **161**, 74
- Oden S. J., et al., 2025, *MNRAS*, submitted, p. arXiv:2512.04200
- Olsen K. A. G., Zaritsky D., Blum R. D., Boyer M. L., Gordon K. D., 2011, *ApJ*, **737**, 29
- Pieres A., et al., 2017, *MNRAS*, **468**, 1349
- Price-Whelan A. M., 2017, *The Journal of Open Source Software*, 2
- Price-Whelan A. M., Nidever D. L., Choi Y., Schlafly E. F., Morton T., Koposov S. E., Belokurov V., 2019, *ApJ*, **887**, 19
- Price-Whelan A. M., et al., 2023, adrn/gala: v1.7.1, doi:10.5281/zenodo.8217584, <https://doi.org/10.5281/zenodo.8217584>
- Putman M. E., et al., 1998, *Nature*, **394**, 752
- Putman M. E., Staveley-Smith L., Freeman K. C., Gibson B. K., Barnes D. G., 2003, *ApJ*, **586**, 170
- Růžička A., Theis C., Palouš J., 2010, *ApJ*, **725**, 369
- Saha A., et al., 2010, *AJ*, **140**, 1719
- Saroon S., Subramanian S., 2022, *A&A*, **666**, A103
- Sheng Y., Ting Y.-S., Xue X.-X., Chang J., Tian H., 2024, *MNRAS*, **534**, 2694
- Stadel J. G., 2001, PhD thesis, University of Washington, Seattle
- Syer D., Tremaine S., 1996, *MNRAS*, **282**, 223
- Theis C., 1999, *Reviews in Modern Astronomy*, **12**, 309

This paper has been typeset from a *T_EX/L_AT_EX* file prepared by the author.